

Heterojunction interfacial metallization effects on carrier dynamics in Te-Sebased infrared photodiodes: An atomic-resolution structure—property study

Zunyu Liu^{1,§}, Meng Peng^{1,2,6,§}, Ziyang Huang⁵, Yuxuan Hu^{1,3}, Huaiyuan Wang⁵, Maohua Chen¹, Shuwen Yan^{1,2}, Mingyang Liu¹, Ning Ma¹, Jingshu Zhang^{1,2}, Chao Chen^{1,2,3,4} (\square), Yihua Gao¹, Shuangfeng Jia⁵, Jianbo Wang⁵, Luying Li¹(\square), Jiang Tang^{1,2,3,4}

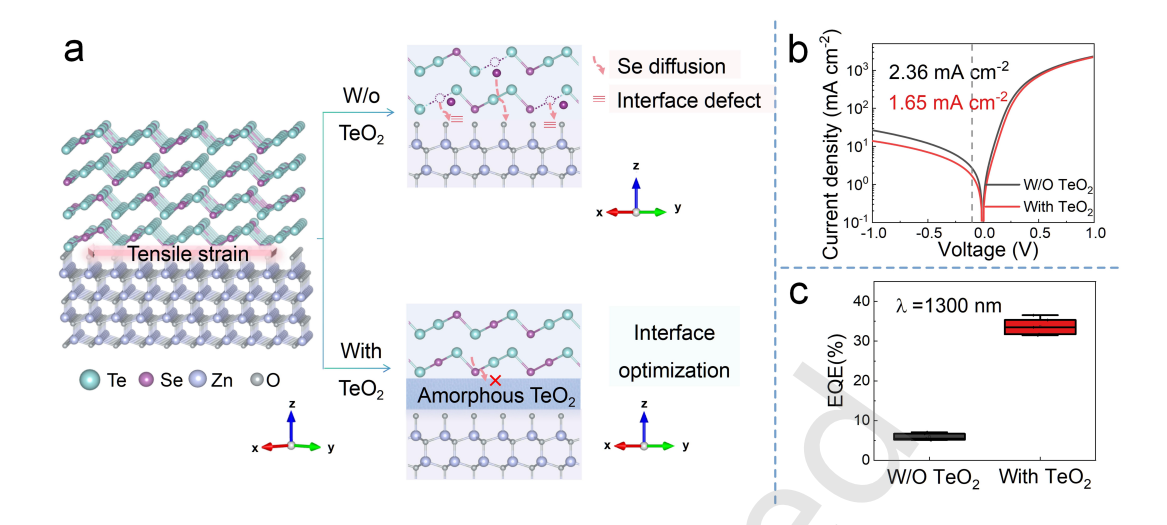
- ¹ Wuhan National Laboratory for Optoelectronics, Huazhong University of Science and Technology, Wuhan 430074, China
- ² School of Optical and Electronic Information, Huazhong University of Science and Technology, Wuhan 430074, China
- ³ China-EU Institute for Clean and Renewable Energy, Huazhong University of Science and Technology, Wuhan 430074, China
- ⁴ Optics Valley Laboratory, Wuhan 430074, China
- ⁵ Center for Electron Microscopy, MOE Key Laboratory of Artificial Micro- and Nano-Structures and the Institute for Advanced Studies, School of Physics and Technology, Wuhan University, Wuhan 430072, China
- ⁶ School of Microelectronics, Wuhan Textile University, Wuhan 430200, China

Nano Res., Just Accepted Manuscript • https://doi.org/10.26599/NR.2025.94908026 https://www.sciopen.com/journal/1998-0124 on Sep. 1, 2025

© The Authors(s)

Just Accepted

This is a "Just Accepted" manuscript, which has been examined by the peer-review process and has been accepted for publication. A "Just Accepted" manuscript is published online shortly after its acceptance, which is prior to technical editing and formatting and author proofing. Tsinghua University Press (TUP) provides "Just Accepted" as an optional and free service which allows authors to make their results available to the research community as soon as possible after acceptance. After a manuscript has been technically edited and formatted, and the page proofs have been corrected, it will be removed from the "Just Accepted" web site and published officially with volume and article number (e.g., Nano Research, 2025, 18, 94906990). Please note that technical editing may introduce minor changes to the manuscript text and/or graphics which may affect the content, and all legal disclaimers that apply to the journal pertain. In no event shall TUP be held responsible for errors or consequences arising from the use of any information contained in these "Just Accepted" manuscripts. To cite this anuscript please use its Digital Object Identifier (DOI®), which is identical for all formats of publication.



This study investigates the effect of interfacial electric field redistribution caused by interfacial metal phase transition on the performance of Te-Se alloy-based shortwave infrared photodiode under high interfacial stress conditions. Microscopic analysis of the Te_{0.6}Se_{0.4}/ZnO interface reveals that stress at the boundary induces the diffusion of Se atoms into the ZnO region, leading to the formation of a new Te-rich metallic phase of Te_{0.75}Se_{0.25}. This metallic phase would significantly impede carrier migration and negatively impact the photoelectric performance of the device. The incorporation of a TeO₂ modified layer would reduce interface stress, and avoid the formation of the metallic phase, which notably reduces dark current and enhances quantum efficiency. This study explores how interfacial stress influences the structure-property relationship of TeSe/ZnO heterojunctions, offering a novel approach to optimizing interface engineering for Te-based infrared detectors.

Research Article

Heterojunction interfacial metallization effects on carrier dynamics in Te-Se based infrared photodiodes: An atomic-resolution structure—property study

Zunyu Liu^{1,§}, Meng Peng^{1,2,6,§}, Ziyang Huang⁵, Yuxuan Hu^{1,3}, Huaiyuan Wang⁵, Maohua Chen¹, Shuwen Yan^{1,2}, Mingyang Liu¹, Ning Ma¹, Jingshu Zhang^{1,2}, Chao Chen^{1,2,3,4,*}, Yihua Gao¹, Shuangfeng Jia⁵, Jianbo Wang⁵, Luying Li^{1,*}, and Jiang Tang^{1,2,3,4}

¹Wuhan National Laboratory for Optoelectronics, Huazhong University of Science and Technology, Wuhan 430074, China

²School of Optical and Electronic Information, Huazhong University of Science and Technology, Wuhan 430074, China

³China-EU Institute for Clean and Renewable Energy, Huazhong University of Science and Technology, Wuhan 430074, China

⁴Optics Valley Laboratory, Wuhan 430074, China

⁵Center for Electron Microscopy, MOE Key Laboratory of Artificial Micro- and Nano-Structures and the Institute for Advanced Studies, School of Physics and Technology,

Wuhan University, Wuhan 430072, China

⁶School of Microelectronics, Wuhan Textile University, Wuhan 430200, China

Received: 10 July 2025; Revised: 28 August 2025; Accepted: 1 September 2025

*Address correspondence to Chao Chen, cchen@mail.hust.edu.cn; Luying Li, luying.li@hust.edu.cn

 Cite
 this
 article:
 Nano
 Research,
 2025,
 18,
 94908026.

 https://doi.org/10.26599/NR.2025.94908026

Abstract

This study investigates the effect of interfacial electric field redistribution caused by interfacial metal phase transition on the performance of Te-Se alloy-based shortwave infrared

photodiode under high interfacial stress conditions. Microscopic analysis of the Te_{0.6}Se_{0.4}/ZnO interface reveals that stress at the boundary induces the diffusion of Se atoms into the ZnO region, leading to the formation of a new Te-rich metallic phase of Te_{0.75}Se_{0.25}. This metallic phase would significantly impede carrier migration and negatively impact the photoelectric performance of the device. The incorporation of a TeO₂ modified layer would reduce interface stress, and avoid the formation of the metallic phase, which notably reduces dark current and enhances quantum efficiency. This study explores how interfacial stress influences the structure-property relationship of TeSe/ZnO heterojunctions, offering a novel approach to optimizing interface engineering for Te-based infrared detectors.

1 Introduction

Tellurium (Te), an elemental p-type semiconductor with one-dimensional helical chains bonded via van der Waals interactions, addresses a critical challenge in semiconductor technology—the scarcity of high-performance p-type materials. Unlike conventional p-type oxides limited to mobilities below 20 cm²-V¹-·s¹-1, the unique chain structure of Te significantly contributes to its high hole mobility (exceeding 1000 cm²-V¹-·s¹-1) at room temperature with anisotropic electronic properties[1]. Furthermore, this chain structure enhances thermoelectric performance by reducing thermal conductivity, improves mechanical properties thanks to the inherent flexibility of the chains, and boosts optoelectronic performance by enabling strong light absorption and efficient photocarrier generation across a wide spectral range.[2-9]. Consequently, Te holds significant potential for applications in electronics, optoelectronics, and thermoelectrics[4, 10, 11]. However, its narrow bandgap (~0.35 eV) makes it easier to generate electron-hole pairs through thermal excitation at room temperature, resulting in high dark current in photodetectors, which limits its device performance.

To address this issue, the formation of Te_xSe_{1-x} alloys, utilizing wide bandgap selenium (Se, 1.9 eV), has emerged as a viable strategy to enhance the device performance[12, 13]. The Te_xSe_{1-x} alloys have been reported to show several advantages: i) The bandgap can be tuned between 0.35 and 1.95 eV by adjusting the Te/Se ratios, allowing bandgap flexibility while retaining strong optical absorption and high hole mobility[3, 13]. ii) The Te_xSe_{1-x} alloys retain the unique

one-dimensional helical chain structure, which reduces the presence of dangling bonds, lowers defect density, and enhances mechanical flexibility, which would further improve its adaptability[14-16]. iii) Te_xSe_{1-x} alloys have low melting point (220 - 450 °C) and low crystallization temperature (< 165°C), making them compatible with deposition techniques like thermal evaporation and physical vapor deposition (PVD), which supports large-scale integration and compatibility with silicon-based device manufacturing[17-19]. Thus, the Te_xSe_{1-x} alloy exhibits notable features, including an adjustable band gap, high mobility, and low-temperature manufacturing capabilities for infrared detection. Its overall performance generally surpasses that of organic materials, quantum dots, and perovskite materials in key metrics for infrared detection. Additionally, the flexibility of Te-Se alloys, the stability achieved through defect control, and their compatibility with silicon circuits enable high-speed, broad-spectrum applications (ranging from 300 to 1800 nm) in cost-effective imaging and wearable devices. Early developments in Te-based photodetectors demonstrated both the promise and challenges of this material platform. In 2014, He et al. pioneered Te photoconductive devices by growing Te nanoplates on flexible mica substrates, achieving a dark current of 25 A cm⁻² under 1 V bias[20]. In 2022, Hu et al. developed a photovoltaic heterojunction device combining Te with graphene[21], reducing the response time to 28 µs but still exhibiting a high dark current of 45 A cm⁻² under -0.1 V bias. To facilitate the integration of Te-based photodetectors with complementary metal-oxide-semiconductor (CMOS) technology, our group initially proposed a thin-film Te-Se alloy photodiode and verified its compatibility with CMOS processes, demonstrating low-power operation and potential for integration with active-matrix substrates. In 2023, Fu et al. reported that the dark current of these thin-film Te-Se alloy photodiodes had been reduced to 3.6×10^{-4} mA cm⁻² under -0.1 V bias, with a response time of 1.2 µs[14]. Subsequently, Lin et al. achieved a response time of 850 ns by further optimization, but the dark current was about 50×10^{-4} mA cm⁻² under -0.1 V bias[6]. Obviously, the high dark current of Te_xSe_{1-x} alloy remains a significant challenge that must be addressed to advance the practical application of related CMOS readout circuits. Despite theoretical predictions that built-in electric fields at heterojunction interfaces should effectively separate photogenerated carriers and reduce dark current, these experimental results consistently demonstrate that interface-related phenomena fundamentally limit device performance, regardless of advances in material synthesis or device architecture.

For now, the persistent challenges in pure Te devices have motivated the development of Te-Se alloys, which offer improved bandgap tunability and enhanced stability over elemental Te. However, even these material advances remain constrained by interface defect-induced excessive dark current in practical applications. A fundamental limitation lies in the unexplored atomic-scale mechanisms governing interfacial stability within TeSe/oxide heterojunctions. This critical knowledge gap has impeded the development of rational interface engineering strategies, leading to a reliance on empirical device-level optimizations that fail to address the root causes of performance limitations. Critically, the absence of systematic atomic-resolution studies on TeSe alloy interfaces represents a major barrier to advancing photodetector technology. Without a comprehensive atomic-scale understanding of structure-property relationships, interface engineering persists as a trial-and-error approach- a constraint that becomes increasingly acute as the field approaches the performance ceiling achievable through conventional optimization methods.

This study bridges the critical knowledge gap through the first atomic-resolution investigation of Te_{0.6}Se_{0.4}/ZnO heterointerfaces under interfacial stress. By combining advanced electron microscopy (HAADF-STEM, DPC) and first-principles calculations, we uncover a stress-driven interfacial metallization mechanism: lattice mismatch and thermal stress induce Se diffusion into ZnO, forming a metallic Te_{0.75}Se_{0.25} phase that distorts local electric fields and elevates dark current. To counteract this, we develop an amorphous TeO₂ modification strategy that simultaneously functions as a strain-relief buffer and diffusion barrier. This approach suppresses phase transformation, achieving reduction in dark current (1.65 × 10⁻² mA cm⁻² at -0.1 V) and 7-fold enhancement in quantum efficiency (35% at 1300 nm). These findings establish atomic-scale interface strain engineering as a universal paradigm for high-performance Te-based infrared photodetectors.

2 Experimental

2.1 Material Preparation

0.53 g of Se powder (99.99%, Sigma Aldrich) and 0.8 g of Te powder (99.999%, Sigma Aldrich) were individually loaded into two separate quartz crucibles. An additional 0.1 grams of

TeO₂ was placed in a third crucible. To ensure uniform heating, all powders in crucibles were thoroughly shaken.

2.2 Device Fabrication

The ITO glass (Liaoning Best New Energy Technology Co. Ltd) was subjected to ultrasonic cleaning with acetone, isopropanol, and ethanol, each for a duration of 15 minutes. Then, a zinc oxide layer of approximately 200 nm thick was deposited on the ITO glass using magnetron sputtering. The deposition of TeO₂ thin films was carried out selectively based on whether surface modified had been implemented. TeO₂ thin films, with a thickness of 0.3 nm, were deposited through thermal evaporation, employing TeO₂ powder as the raw material (3×10^{-4} Pa, 0.1 Å s⁻¹). Subsequently, the prepared Se powder and Te powder served as raw materials for the preparation of Te_{0.6}Se_{0.4} thin films. These films were created via thermal evaporation (1.5×10^{-4} Pa; Se ≈ 1.6 Å s⁻¹, Te ≈ 2.4 Å s⁻¹), resulting in films with a thickness of 400 nm. The as-deposited Te_{0.6}Se_{0.4} thin films were subjected to annealing at 260 °C for 5 minutes using a hot plate (JW-600DG, Wuhan JunWei Co. Ltd). This annealing process was conducted within a nitrogen glove box to mitigate the risk of oxidation of the Te_{0.6}Se_{0.4} film. Following this, an 80 nm gold electrode was thermally evaporated (using TEMD-600, Technol Science) onto the annealed Te_{0.6}Se_{0.4} film to fabricate a complete infrared photodetector.

2.3 Device Characterizations

C-V measurements were conducted at 25 °C within an electromagnetic shielding box, employing a frequency of 100 kHz and an AC amplitude of 30 mV. The DC bias voltage was swept from -1.0 to 1.0 V. The EQE values were determined using a semiconductor analyzer (Agilent B1500A) and a quantum efficiency measurement system (Enlitech QE-R).

2.4 Materials Characterizations

The cross-sectional TEM samples of the devices were sliced by focused ion beam (FIB) using Helios 5. The HRTEM images, HAADF-STEM images for structural characterization and DPC maps for electrical analysis were obtained by the JEM-ARM200CF with double Cs-corrector and segmented STEM detector operated at 200 kV. XRD spectra were measured with an X-ray diffractometer (Bruker, D2 Phaser with Cu-K α (λ = 1.5405 Å) radiation) at room temperature in the 2 θ range of 20°–80°.

2.5 Theoretical calculation

First-principles calculations were conducted using the Vienna Ab-initio Simulation Package (VASP). The interactions between the core ions and valence electrons were modeled using the projector augmented-wave (PAW) pseudopotential, while the exchange-correlation functional was approximated using the generalized gradient approximation (GGA) within the Perdew-Burke-Ernzerhof (PBE) framework. For the self-consistent calculations, k-point sampling was performed using the Monkhorst-Pack scheme, with a grid of $9 \times 9 \times 9$. The plane-wave energy cutoff was set to 600 eV. The convergence criteria for the total energy were set to a tolerance of 1×10^{-7} eV per atom, with a maximum force tolerance of 1.0×10^{-3} eV·Å⁻¹.

3 Results and discussion

3.1 Interface Stress Problems and Solutions

The integration of mismatched materials in semiconductor heterostructures presents a fundamental challenge for interface engineering. When forming high-quality heterojunctions, interfacial stress — originating from disparities in thermal expansion coefficients and lattice parameters between constituent materials — often compromises device integrity. Such stresses drive atomic diffusion, phase transformations, and defect formation, ultimately degrading performance through increased recombination centers and altered band alignments.

In TeSe alloy-based photodetectors, interface-related challenges are particularly pronounced due to the unique one-dimensional chain structure of these materials and their growth on conventional oxide buffer layer. Previous research has demonstrated that thermal processing induces significant interfacial reactions and atomic diffusion at TeSe/oxide interfaces, leading to degraded device performance. To systematically investigate these phenomena, this study focuses on the Te_{0.6}Se_{0.4}/ZnO heterointerface as a model system, examining the fundamental mechanisms of stress-induced structural transformations and their impact on photodetector performance.

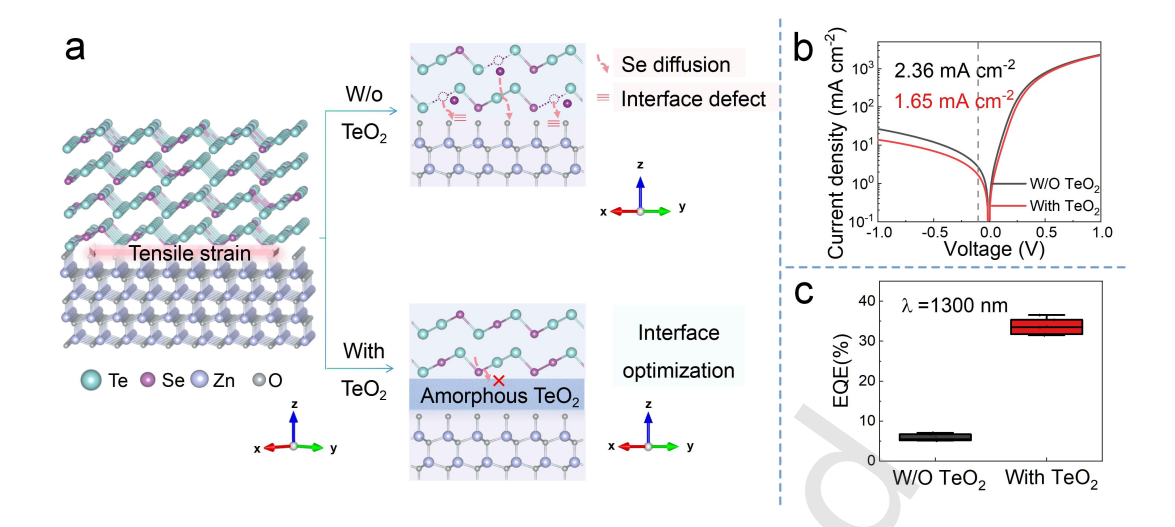


Figure 1 Interface Stress Problems and Solutions. (a) The atomic model of Te-Se alloy/ZnO hetero-interface (left), the atomic models of the Te-Se alloy/ZnO interface with (lower) or without (upper) TeO₂ modified layer, focusing on the effects of Se diffusion and interface defect. (b,c) Dark current density versus different voltages (Jd - V curve) and the external quantum efficiency (EQE) spectra of devices with and without TeO₂ modification.

The interfacial stress in thin-film heterojunctions is predominantly composed of thermal stress and lattice mismatch stress[22, 23]. Thermal stress arises at the interface due to differences in the thermal expansion properties of the constituent materials. When subjected to a temperature gradient during annealing and cooling processes, ranging from 260°C to room temperature, significant thermal stress differences are observed between the Te_{0.6}Se_{0.4} alloy and ZnO polycrystalline material. Specifically, the thermal stress in the Te_{0.6}Se_{0.4} alloy is as high as 72 MPa, whereas that in ZnO polycrystalline material is much higher, reaching 249.6 MPa[24-28]. For detailed calculations, please refer to Note S1. This disparity is primarily attributed to the considerably higher elastic modulus of ZnO, despite the relatively small difference in their thermal expansion coefficients. The resulting stress difference at the interface has a substantial impact on the performance of the heterojunction.

Lattice mismatch is another major source of interfacial stress in thin-film heterojunctions. Through the analysis of X-ray diffraction (XRD) spectra (as shown in Fig. S1), the lattice parameters of the materials are determined, and the $Te_{0.6}Se_{0.4}$ alloy is assumed to have a hexagonal structure with space group of $P3_121$ (152) and lattice parameters of a = b = 0.4420 nm and c = 0.5534 nm. The calculated lattice mismatch between $Te_{0.6}Se_{0.4}$ alloy and ZnO ranges from a

minimum of 5.89 % to a maximum of 31.9 %. The estimated interfacial stress is between 3.08 and 16.69 GPa. For detailed calculations, please refer to Note S2. However, due to phenomena such as dislocation development, elastic relaxation, and plastic deformation, the actual stress caused by lattice mismatch is typically much lower than these estimates[29, 30]. This lattice mismatch stress plays a critical role in stability and performance of the heterojunction.

The combined thermal and lattice mismatch stresses create a complex stress field that fundamentally alters the interfacial structure and composition, as shown in Fig. 1a. This stress-driven instability manifests in several critical ways: (i) atomic diffusion across the interface, leading to compositional gradients and phase separation; (ii) formation of structural defects including dislocations and grain boundaries; and (iii) development of new phases with altered electronic properties. These phenomena collectively degrade photoelectric conversion efficiency and increase dark current through enhanced recombination pathways.

To address these fundamental interface challenges, we developed an amorphous TeO₂ interlayer approach that simultaneously tackles both stress relief and atomic diffusion. The amorphous TeO₂ layer serves multiple functions: (i) providing stress accommodation through its inherent structural flexibility; (ii) acting as a diffusion barrier to prevent Se migration.

Device characterization demonstrates the effectiveness of this approach (Fig. 1b,c). Compared to unpassivated devices, TeO₂-passivated photodetectors exhibit dramatically improved performance: dark current reduction from 2.36 mA cm⁻² to 1.65×10⁻² mA cm⁻² at a bias of -0.1 V, and external quantum efficiency enhancement from ~5% to 35% at 1300 nm illumination at 1300 nm. This substantial performance improvement validates the critical role of interface engineering in realizing high-performance TeSe alloy-based photodetectors and establishes design principles applicable to broader TeSe alloy/oxide heterostructure systems.

3.2 Interface strain analysis

The crystal lattices at the interfaces of the two devices are analyzed to investigate the interfacial strain conditions. Fig. 2a presents a high-resolution transmission electron microscopy (HRTEM) image of the interface between Te_{0.6}Se_{0.4} and ZnO, with the TeSe alloy occupying the upper half and the ZnO located in the lower half. The regions of the TeSe alloy with perfect crystal lattices serve as reference regions to facilitate the comparative strain analyses. Additionally, the

HRTEM image and corresponding FFT of the TeSe alloy are also depicted in Fig. S3. It can be concluded that the crystal structure of the TeSe alloy belongs to hexagonal system, consistent with previous studies. The structure of TeSe alloy can maintain its stability under minimal or no applied stress.

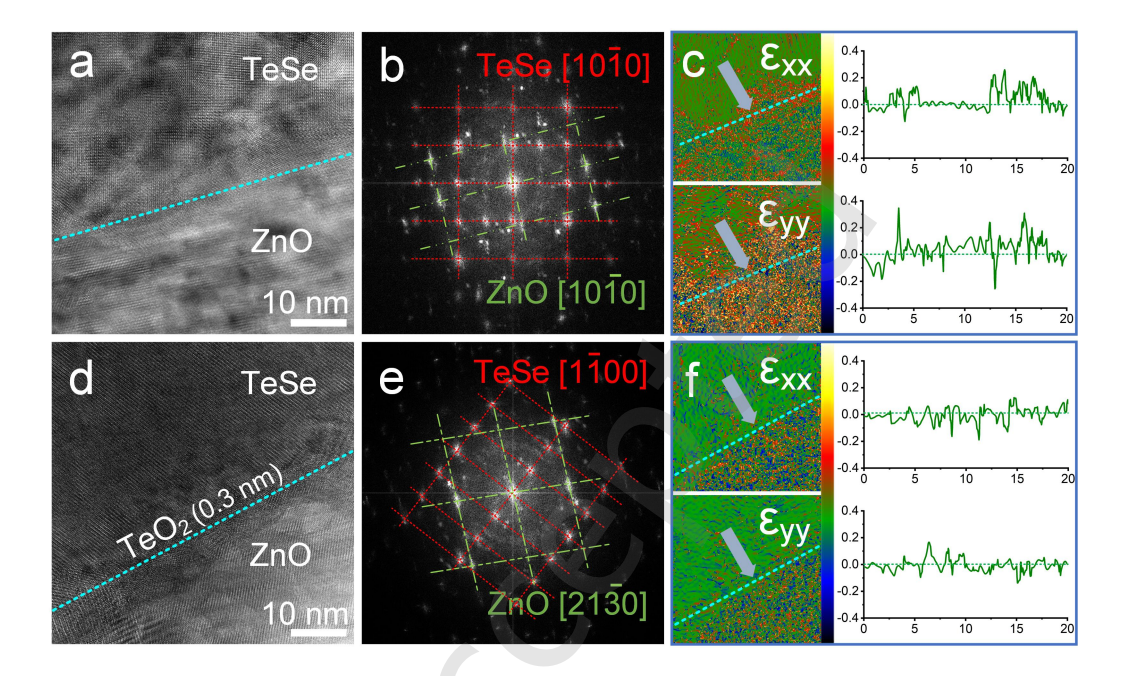


Figure 2 Interface strain conditions with or without the amorphous TeO₂ layer. (a) The HRTEM image of TeSe alloy/ZnO heterojunction. (b,c) The FFT and strain map related to (a). (d) The HRTEM image of the heterojunction with the introduction of an amorphous TeO₂ layer. (e,f) The FFT and strain map related to (d).

However, the crystal lattice of TeSe alloy at the TeSe/ZnO interface differs from that in the bulk region, as evidenced by the HRTEM image at the TeSe-ZnO junction (Fig. 2a). As depicted in Fig. 2b of the associated FFT, the diffraction spots for TeSe [1010] and ZnO [1010] are labeled by red and green dotted lines, respectively. Upon subtracting the primary diffraction spots from the FFT, Fig. S4 presents the lattice information obtained from the inverse Fourier transform of the residual diffraction spots. It is evident that significant defects emerge in the TeSe alloy near the interface due to lattice mismatch induced strain. These defects include disordered crystal orientations and crystal twisting, which are commonly observed in regions with high level strain.

Geometric phase analysis is employed to quantitatively characterize the interface strain

distribution, with the assumption that the region of TeSe alloy far from the interface in Fig. 2b serves as the reference region with zero strain field. This strain distribution defines the displacements of the deformed lattices relative to the selected reference region, as illustrated in Fig. 2c. The normal strain components are displayed along the vertical (i.e., the out-of-plane component ε_{yy}) and horizontal (i.e., the in-plane component ε_{xx}) directions. Noticeable fluctuations in both strain line profiles of TeSe alloy are observed near the interface. Figure 2d presents the high-resolution transmission electron microscopy (HRTEM) image of the TeSe/ZnO interface, which is characterized by a 0.3 nm amorphous TeO₂ passivation layer. The presence and thickness of the TeO₂ layer were further verified through high-angle annular dark-field (HAADF) imaging, which revealed the presence of 1-3 amorphous atomic layers at the interface (Fig. S5). The corresponding FFT in Fig. 2e shows much less diffuse diffraction spots as compared to that lacking the TeO₂ layer, indicating higher level of single crystallinity of the interfacial structure. Fig. S4b is the inverse Fourier transform of the diffuse diffraction spots, it is evident that the ZnO region located in the lower right corner of Fig. 2d is the main contributor to the disordered crystal structures. Additionally, the corresponding strain maps and line profiles in Fig. 2f also present much lower levels of interfacial strain. Thus, it can be concluded that the amorphous TeO₂ layer serves to release the interfacial strain due to lattice mismatch, and maintain the original atomic arrangements of TeSe alloy at the interface.

3.3 Atomic structure of the stress-affected interface region

It is well established that lattice mismatch would induce strain field at the TeSe/ZnO heterointerface. However, the effects of the strain field at the atomic level remain inadequately understood. Figs. 3a and 3d are atomic-resolution high-angle annular-dark-field (HAADF) images of the TeSe region along two different crystal orientations. The interface can be broadly categorized into three distinct regions—upper, middle, and lower—based on the overall atomic arrangements and elemental distributions, as depicted in Figs. 3g, 3h, and S6. Specifically, the lower section corresponds to the ZnO region, while the upper and middle sections correspond to the TeSe region.

The HAADF images obtained in scanning transmission electron microscopy (STEM) mode

reflect the Z-contrast of each atomic column. The atomic arrangements along the hexagonal TeSe $[10\overline{1}0]$ and $[12\overline{3}2]$ zone axes are depicted in the upper half of Figs. 3a and 3d, respectively. The corresponding FFTs of the blue dashed box regions are presented in Figs. 3b and 3e, respectively. The diffraction spot indexing was based on d-spacing measurements obtained from HR-TEM lattice imaging, with detailed analysis provided in Figure S7. For the lower half region, the atomic resolution HAADF images and corresponding FFTs of the purple dashed box regions reveal different atomic configurations as compared to those of the upper region, and this novel phase of TeSe has not been found in existing literature. To assess the repeatability of the experiment, additional experimental data from two independent $Te_{0.6}Se_{0.4}$ / ZnO heterostructure samples, prepared under identical conditions, have been included in the supplementary information(Fig. S8). At the intermediate region between the original and new phase of TeSe, several dislocations are observable to alleviate internal stress within the material. The formation of the new TeSe phase is also a direct consequence of the high-level interfacial stress.

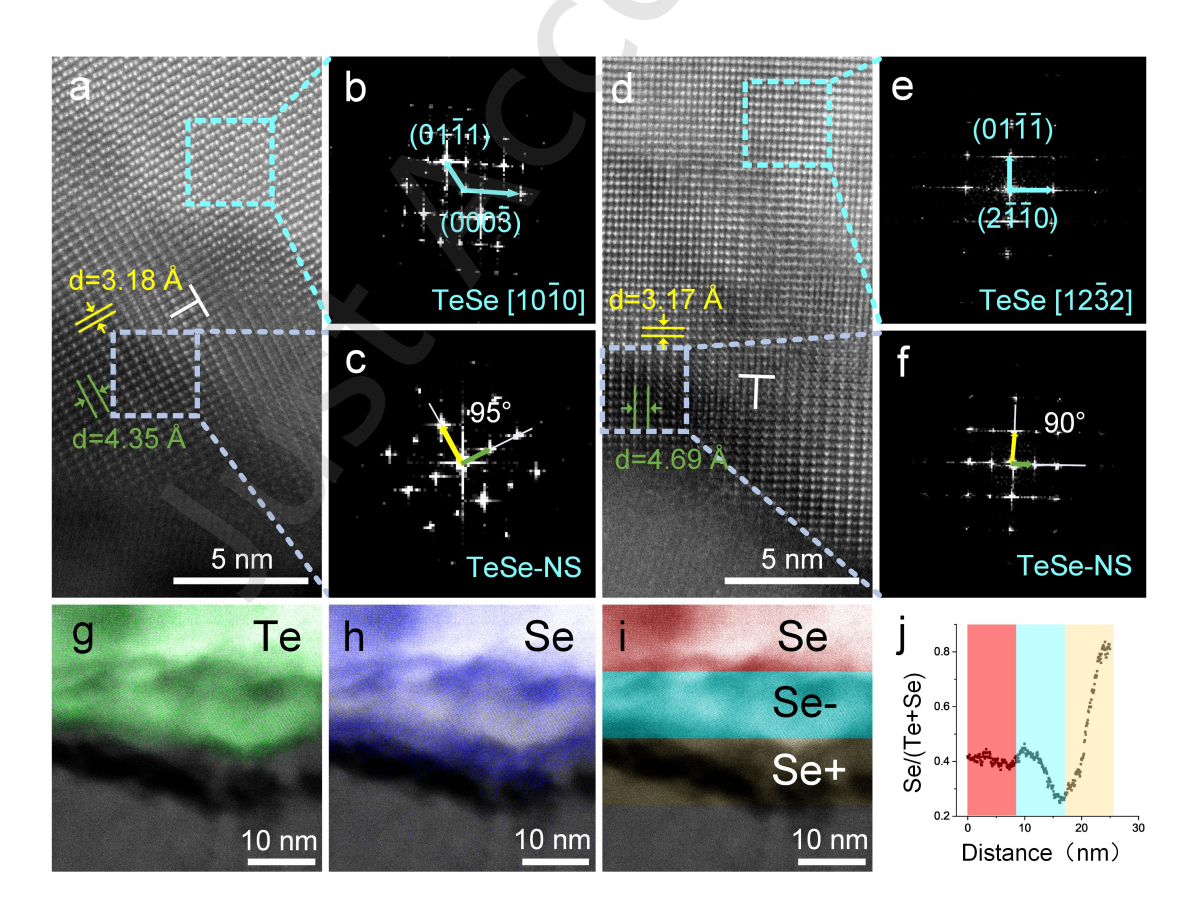


Figure 3 Atomic structure and elemental distribution at TeSe/ZnO heterojunction. (a) The atomic resolution HAADF image of the TeSe/ZnO interface with the TeSe alloy of hexagonal structure

along $[10\overline{1}0]$ zone axis. (b,c) The corresponding FFTs of the blue and purple dashed box regions in (a), respectively. (d) The atomic resolution HAADF image of the interface region with the hexagonal TeSe along $[12\overline{3}2]$ zone axis. (e,f) The corresponding FFTs of the blue and purple dashed box regions in (d), respectively. (g,h) Elemental distribution of Te and Se at the interface as determined by EDS. i The red, blue and yellow bands label the original TeSe region, Se-deficient region and Se-rich region, respectively. (j) Line profile showing the composition ratio of Se/(Se+Te) at the interface.

Furthermore, the concentrations of Te and Se are quantitatively analyzed across the TeSe/ZnO hetero-interface based on the data extracted from the EDS elemental maps of Te and Se (Figs. 3g-h). This approach facilitates calculation of the compositional ratio of Se/(Te+Se) present at the interface, as depicted in Fig. 3j. The ratio of Se/(Te+Se) within the red region of Fig. 3i, which corresponds to the hexagonal structure of TeSe, is determined to be 0.4. The concentration ratio of Se in the blue region of Fig. 3i gradually decreases to approximately 0.25, which coincides with the region associated with the new TeSe phase. Conversely, the ratio increases abruptly in the yellow area corresponding to the adjacent ZnO, which reflects the diffusion of Se to the ZnO region with Te left behind.

It is apparent that Se atoms are inclined to diffuse in the interface region, which is beneficial for the formation of the new TeSe phase. Substantial strain fields exist at the interface due to the considerable lattice mismatch between TeSe and ZnO. To alleviate this high-level strain, Se atoms are driven to diffuse into the ZnO region, leading to the formation of the new TeSe phase.

3.4 Analysis of TeSe's novel phase

This section primarily focuses on the unit cell structure of the novel phase. The FFTs of the novel phase in the white dashed box regions in Figs. 3a and 3d are depicted in Figs. 3c and 3f, respectively. The angle between the two primary crystal planes in Fig. 3c is measured to be 95°, while the angle between the two principal crystal planes in Fig. 3f is 90°. Additionally, the $[10\overline{1}0]$ direction is perpendicular to the $[12\overline{3}2]$ direction for the hexagonal TeSe in the upper regions of Figs. 3a and 3d, with $\{01\overline{1}1\}$ crystal planes parallelling to both zone axes. Thus, Fig. 3d can be derived from Fig. 3a by rotating the crystal 90° around the normal axis of $\{01\overline{1}1\}$ plane. The

reciprocal lattice vectors indicated by the yellow arrows in Figs. 3c and 3f are perpendicular to the $\{01\overline{1}1\}$ crystal planes of hexagonal TeSe. Based on the above analysis, the unit cell structure of the novel phase is characterized as belonging to the monoclinic crystal system.

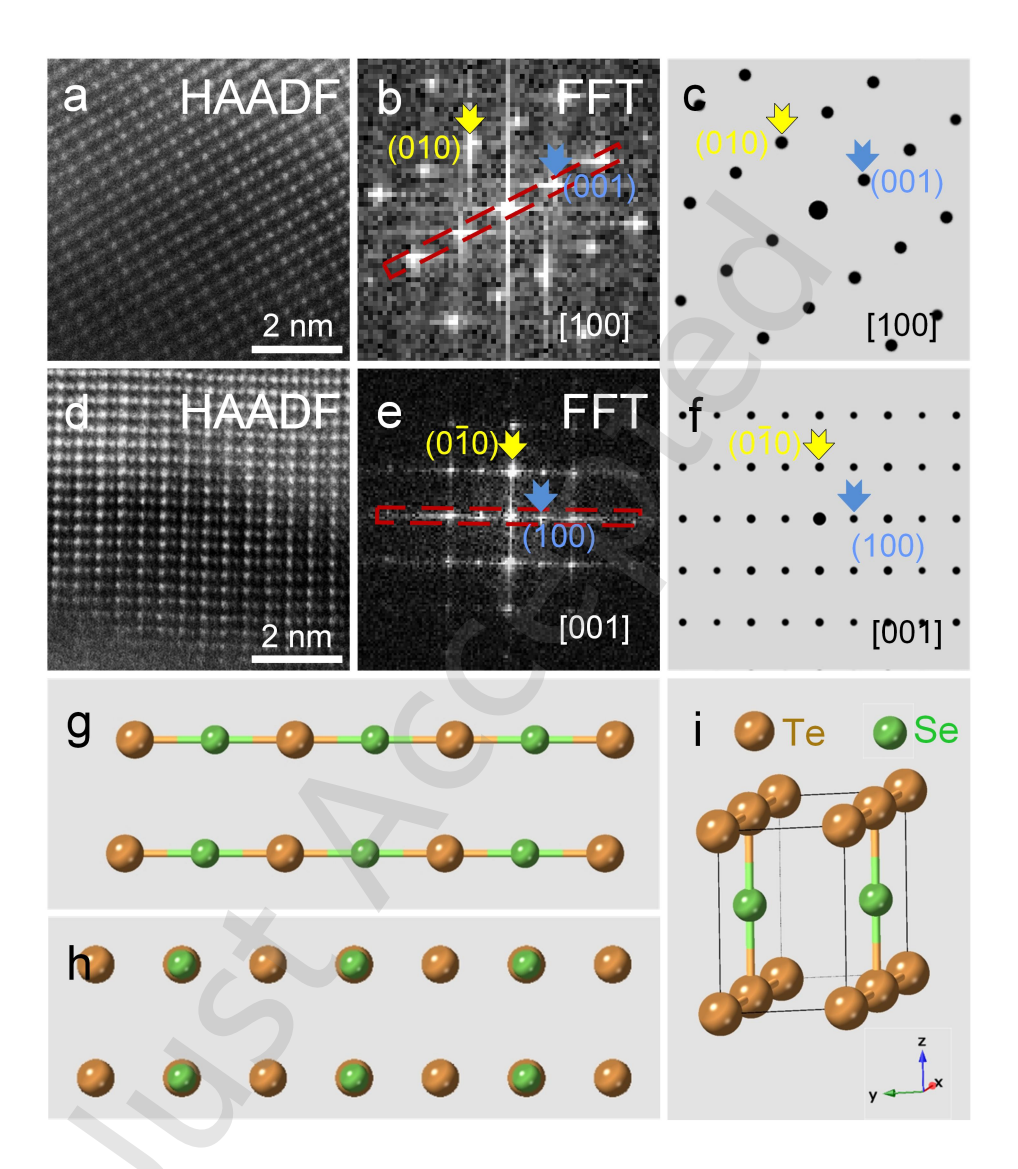


Figure 4 Analysis of the Novel Phase Structure of TeSe. (a) Amplified image of the newly identified phase structure region of TeSe in Fig. 3a. (b) The corresponding FFT of (a). (c) Simulated diffraction pattern of the [100] zone axis based on the computed lattice parameters of the unit cell. (d) Amplified image of the newly identified phase structure region of TeSe in Fig. 3d. (e) The corresponding FFT of (d). (f) Simulated diffraction pattern of the [001] zone axis based on the computed lattice parameters of the unit cell. (g,h) The schematic diagrams depicting the atomic arrangements along the [100] and [001] zone axes of the newly identified TeSe phase structure, respectively. (I) Three-dimensional atomic model showing the unit cell structure of the newly identified TeSe phase.

The interfacial region of the Te_{0.6}Se_{0.4}/ZnO heterojunction was examined using HAADF

imaging to uncover the structural changes induced by interfacial strain. As shown in Fig. 4a, the atomic arrangements in the interfacial region deviate significantly from the hexagonal symmetry observed in the bulk TeSe alloy. The HAADF image reveals alternating bright and dim atomic columns, corresponding to Te-rich and Se-rich regions, suggesting a periodic modulation of the Te/Se stoichiometry. Fast Fourier transform (FFT) analysis of this region (Fig. 4b) confirms the presence of additional diffraction spots not observed in the bulk material, indicating the formation of a new crystallographic phase. Similarly, the HAADF image in Fig. 4d, taken from a different zone axis, further supports the existence of this new phase, with the corresponding FFT pattern (Fig. 4e) showing distinct diffraction features.

To precisely determine the structural parameters of the new phase, the FFT patterns were compared with simulated diffraction patterns derived from the assumed unit cell model. The simulated diffraction patterns for specific crystallographic directions (Figs. 4c,f) exhibit excellent agreement with the experimental FFT patterns (Figs. 4b,e), enabling the determination of the unit cell parameters: a = 0.474 nm, b = 0.314 nm, c = 0.440 nm, with angles $\alpha = 95^{\circ}$, $\beta = \gamma = 90^{\circ}$ (Fig. 4i). The interplanar spacing of 0.317-0.318 nm of the {010} planes (Fig. 4a) exceeds the covalent bond length of Te (0.283 nm), suggesting that van der Waals interactions would dominate the interlayer stabilization-a feature contrasting sharply with the covalent bonding in conventional hexagonal TeSe alloys.

Atomic projection models along the [100] and [001] directions (Figs. 4g,h) demonstrate periodic arrangement of Te and Se atoms. The three-dimensional unit cell structure (Fig. 4i) highlights the monoclinic symmetry and unique stacking sequence of the new phase. It is expected that the stoichiometric change, driven by the diffusion of Se atoms into the ZnO layer, destabilizes the hexagonal TeSe structure and promotes the formation of the monoclinic phase. The new phase acts as a structural buffer to relieve the interfacial strain, but its presence would have profound implications for the electronic properties of the heterojunction, as discussed in subsequent sections.

3.5 Optimized interface atomic arrangements

To determine if the formation of the novel phase is directly linked to the strain field at the interface, it is necessary to analyze the interfacial atom arrangements of the optimized device with a thin TeO₂ layer insertion. HAADF images of the hexagonal TeSe/ZnO interface, with the TeSe regions captured along the [0001] and [21\overline{3}0] zone axes, are presented in Figs. 5a and 5c, respectively. The corresponding FFTs of the blue dashed boxes are illustrated in Figs. 5b and 5d. Both Fig. 5a and Fig. 5c clearly indicate that no novel phase of TeSe is present at the hexagonal TeSe/ZnO interface. This observation illustrates that the thin TeO₂ layer provides effective physical separation, thereby reducing interfacial strain.

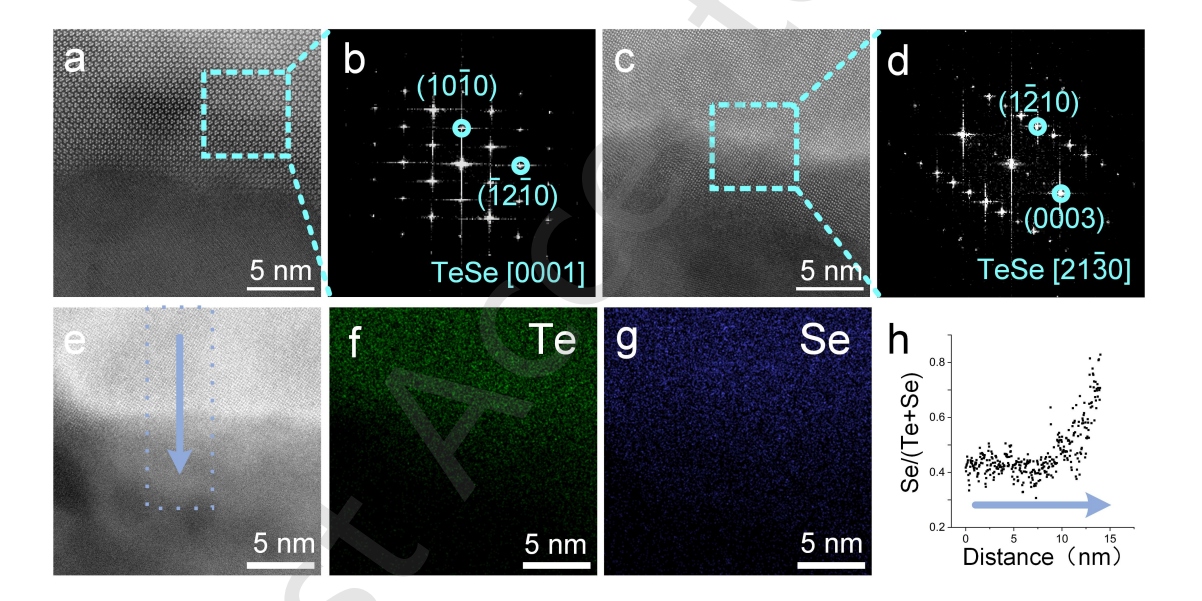


Figure 5 Characterization of the atomic arrangements at the interface of the optimized device. (a,c) HAADF images of hexagonal TeSe/ZnO interfaces, with the TeSe regions along [0001] and [2130] zone axes, respectively. (b,d) The corresponding FFTs of the blue dashed boxes in (a) and (c), respectively. (e-g) HAADF image of the interfacial region and corresponding EDS elemental maps of Te and Se. (h) The line profile showing the composition ratio of Se/(Te+Se) in the blue box illustrated in (e).

The HAADF image of the hexagonal TeSe/ZnO interface, and the EDS elemental maps of Te and Se, are presented in Figs. 5e-g, and the elemental signals for Te and Se have been normalized. As illustrated in Fig. 5h, although the diffusion of Se into the ZnO region still exists, the concentration of Se in the TeSe region remains consistent near the interface. This phenomenon can be attributed to the ability of the TeO₂ layer to largely inhibit Se atom diffusion. Moreover, the

amorphous nature of the TeO₂ layer would mitigate the interface strain, which would otherwise facilitate Se diffusion. Thus, this again proves that the strain field experienced by the interface and the generation of the novel phase are interconnected, and the diffusion of Se could be a critical factor in the formation of the novel TeSe phase.

3.6 Electrical properties of the novel TeSe phase at atomic resolution

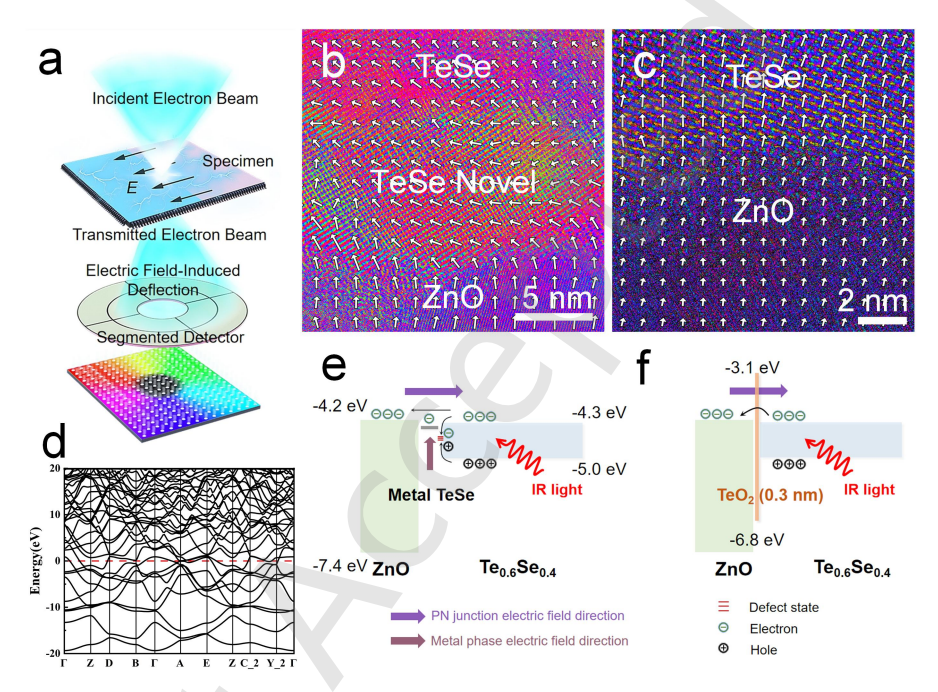


Figure 6 Analysis of electrical properties of the interfaces at atomic resolution. (a) Schematic diagram of DPC-STEM technique. (b,c) The distribution of electric fields at the TeSe/ZnO interface without and with the insertion of the TeO₂ layer, respectively. (d) The energy band diagram of Te_{0.75}Se_{0.25} (new phase structure) obtained by first-principles calculations. (e,f) The interface energy band structure without and with the TeO₂ layer, respectively.

As depicted in Fig. 6a, when the electron beam traverses a sample, the internal electric field of the sample would modulate the phase of the electron wave through quantum mechanical interactions. This phenomenon arises from the Aharonov-Bohm effect, where the phase shift $(\Delta \phi)$ of the electron wave is proportional to the integral of the electrostatic potential (V) along the beam path, enabling direct correlation between phase gradients and electric field distributions. The detection system employs a quadrant-segmented annular detector to capture differential signals

from beam deflection. Through real-time differential phase contrast (DPC) analysis, phase gradient maps are derived by calculating the normalized intensity differences between opposing detector segments (I₁-I₂)/(I₁+I₂). Subsequent integration of these phase gradients can reconstruct the sample's electric potential landscape at nanometer resolution. The vacuum reference region provides baseline calibration, with pseudocolor maps encoding both direction (hue) and magnitude (saturation) of the electric field, while the vector arrow maps quantitatively represent field orientation (direction) and strength (length)[31-33].

When P-type and N-type semiconductor materials form contact, carrier exchange occurs through electron diffusion from the N-type region (high electron concentration) to fill holes in the P-type region, accompanied by hole migration in the reverse direction for recombination. This process generates a built-in electric field oriented from the N-type to P-type region across the PN junction. In the original device, DPC characterization reveals an anomalous electric field distribution at the TeSe/ZnO interface (Fig. 6b). Although the overall field direction remains from the N-type ZnO to the P-type TeSe, localized field deflections are observed within newly formed TeSe phase domains. This abnormal field distribution is presumed to originate from the emergence of a new phase within the TeSe region. Band structure simulations indicate that this new phase corresponds to a metallic Te_{0.75}Se_{0.25} interlayer at the heterojunction interface, whose zero-bandgap characteristic confirms its metallic nature (Fig. 6d).

The conductive metallic phase fundamentally alters the interface electric field through two interrelated mechanisms: First, its inherent screening effect redistributes the built-in electric field, creating non-uniform field lines that deviate from the ideal PN junction configuration (Fig. 6b). Second, the abrupt transition from semiconductor (TeSe/ZnO) to metal (Te_{0.75}Se_{0.25}) introduces unpassivated interface states, enabling direct carrier tunneling between ZnO and TeSe with reduced activation energy (Fig. 6e). Although the metallic layer provides low-resistance in-plane conduction, its presence establishes competing transport pathways—vertical carrier transport becomes dominated by Schottky-like barriers at the metal/semiconductor interfaces, while lateral currents preferentially flow through the metallic phase. This spatial anisotropy induces carrier scattering and recombination at defect sites, ultimately degrading both vertical charge collection efficiency and overall junction rectification.

In contrast, the amorphous TeO₂ modification layer in the optimized device suppresses Se diffusion and interfacial stress, thereby preventing metallic phase formation (Fig. 6c). The restored semiconductor-semiconductor junction exhibits three synergistic improvements in device physics: Continuous built-in electric field enhances drift-dominated carrier transport; preserved P-type TeSe/ZnO band alignment minimizes interfacial states (Fig. 6f); and reduced defect density mitigates recombination losses. Consequently, the TeO₂-modified interface demonstrates superior carrier separation and collection characteristics compared to the metallic phase-dominated original device.

4 Conclusion

This study reveals the crucial role of interface engineering in improving TeSe alloy-based infrared photodetectors, focusing on the impact of Se diffusion and interface strain on device performance. Our results show that thermal stress and lattice mismatch significantly contribute to interfacial strain, promoting Se diffusion into the ZnO region and forming a new metallic phase Te_{0.75}Se_{0.25}, as confirmed by atomic-scale structural analysis and differential phase contrast analysis. This metallic phase alters the electrical properties at the interface, presenting both opportunities and challenges for performance improvement. The introduction of an amorphous TeO₂ modified layer effectively mitigates interfacial strain, reducing dark current and improving external quantum efficiency. This strategy physically separates the TeSe alloy from the ZnO substrate, limiting Se diffusion and preserving the crystal structure's integrity. Comparative analysis of passivated and unpassivated devices indicates that the TeO₂ layer stabilizes the atomic structure at the interface, which is critical for maintaining photodetector performance under high level strain.

Our findings offer new insights into the behavior of the TeSe alloy/ZnO interface, particularly under high strain conditions. The monoclinic phase appearing at the interface suggests that strain-induced phase transformation may affect local carrier dynamics, highlighting the potential of strain control for enhancing device performance. Further research on the atomic arrangement and electronic structure of this phase, along with alternative modified strategies, may provide

better solutions to optimize device stability and efficiency. This study emphasizes the importance of atomic-level control in developing high-performance TeSe alloy-based photodetectors and paves the way for future advancements in semiconductor and optoelectronic devices.

Data availability

All data needed to support the conclusions in the paper are presented in the manuscript and the Electronic Supplementary Material. Additional data related to this paper may be requested fromthecorresponding authorupon request.

Acknowledgments

This work was supported by the National Key Research and Development Program of China (2022YFA1204800, 2023YFB360890 and 2021YFA0715502). This work was financially supported by the National Natural Science Foundation of China (62174064) and the Innovation Project of Optics Valley Laboratory (No. OVL2023ZD002). The authors would like to thank the Analysis and Testing Center of HUST, the Center of Optoelectronic Micro & Nano Fabrication and Characterizing Facility, and the HPC Platform of Huazhong University of Science and Technology for the characterizations and the computation.

Declaration of competing interest

All the contributing authors report no conflict of interests in this work.

Author contribution statement

Z.L. and M.P. contributed equally to this work. Z.H., Y.X., H.W., and M.C. conceived and designed the research. L.L., C.C., Y.G, S.J., J.W. and J.T. led the experiments. S.Y., M.L., N.M., J.Z., Q.Y., Z.L., H.Z., F.X., H.L., Y.C., and T.F. contributed to the fabrication and characterization of actuators. H.C. and L.X. co-wrote the manuscript. All authors read and approved the final manuscript.

Use of AI statement

None.

Reference

- 1. Paterson, A. F.; Singh, S.; Fallon, K. J.; Hodsden, T.; Han, Y.; Schroeder, B. C.; Bronstein, H.; Heeney, M.; McCulloch, I.; Anthopoulos, T. D. Recent Progress in High-Mobility Organic Transistors: A Reality Check. *Advanced Materials* **2018**, *30*, 1801079.
- 2. Zhao, C.; Tan, C.; Lien, D.-H.; Song, X.; Amani, M.; Hettick, M.; Nyein, H. Y. Y.; Yuan, Z.; Li, L.; Scott, M. C., et al. Evaporated tellurium thin films for p-type field-effect transistors and circuits. *Nature Nanotechnology* **2020**, *15*, 53-58.
- 3. Tan, C.; Amani, M.; Zhao, C.; Hettick, M.; Song, X.; Lien, D.-H.; Li, H.; Yeh, M.; Shrestha, V. R.; Crozier, K. B., et al. Evaporated SeTe1- Thin Films with Tunable Bandgaps for Short-Wave Infrared Photodetectors. *Advanced Materials* **2020**, *32*, 2001329.
- 4. Amani, M.; Tan, C.; Zhang, G.; Zhao, C.; Bullock, J.; Song, X.; Kim, H.; Shrestha, V. R.; Gao, Y.; Crozier, K. B., et al. Solution-Synthesized High-Mobility Tellurium Nanoflakes for Short-Wave Infrared Photodetectors. *ACS Nano* **2018**, *12*, 7253-7263.
- 5. Zhang, P.; Liang, Q.; Zhou, Q.; Chen, J.; Li, M.; Deng, Y.; Liang, W.; Zhang, L.; Zhang, Q.; Gu, L., et al. High-performance terahertz modulators induced by substrate field in Te-based all-2D heterojunctions. *Light: Science & Applications* **2024**, *13*, 67.
- 6. Li, R.; Yao, F.; Xu, Y.; Bai, S.; Jia, Z.; Lin, Q. Optimizing the Charge Carrier Dynamics of Thermal Evaporated TexSe1-x Films for High-Performance Short-Wavelength Infrared Photodetection. *Advanced Functional Materials* **2024**, *34*, 2307005.
- 7. Li, L.; Zhao, S.; Ran, W.; Li, Z.; Yan, Y.; Zhong, B.; Lou, Z.; Wang, L.; Shen, G. Dual sensing signal decoupling based on tellurium anisotropy for VR interaction and neuro-reflex system application. *Nature Communications* **2022**, *13*, 5975.
- 8. Xie, Z.; Xing, C.; Huang, W.; Fan, T.; Li, Z.; Zhao, J.; Xiang, Y.; Guo, Z.; Li, J.; Yang, Z., et al. Ultrathin 2D Nonlayered Tellurium Nanosheets: Facile Liquid-Phase Exfoliation, Characterization, and Photoresponse with High Performance and Enhanced Stability. *Advanced Functional Materials* **2018**, *28*, 1705833.
- 9. He, Y.; Hu, Y.; Peng, M.; Fu, L.; Gao, E.; Liu, Z.; Dong, C.; Li, S.; Ge, C.; Yuan, C., et al. One-Dimensional Crystal-Structure Te—Se Alloy for Flexible Shortwave Infrared Photodetector and Imaging. *Nano Letters* **2024**, *24*, 5774-5782.
- 10. Tong, L.; Huang, X.; Wang, P.; Ye, L.; Peng, M.; An, L.; Sun, Q.; Zhang, Y.; Yang, G.; Li, Z., et al. Stable mid-infrared polarization imaging based on quasi-2D tellurium at room temperature. *Nature Communications* **2020**, *11*, 2308.
- 11. Shen, C.; Liu, Y.; Wu, J.; Xu, C.; Cui, D.; Li, Z.; Liu, Q.; Li, Y.; Wang, Y.; Cao, X., et al. Tellurene Photodetector with High Gain and Wide Bandwidth. *ACS Nano* **2020**, *14*, 303-310.
- 12. Reddy, K. V.; Bhatnagar, A. K. Electrical and optical studies on amorphous Se-Te alloys. *Journal of Physics D: Applied Physics* **1992**, *25*, 1810.
- 13. Hadar, I.; Hu, X.; Luo, Z.-Z.; Dravid, V. P.; Kanatzidis, M. G. Nonlinear Band Gap Tunability in Selenium–Tellurium Alloys and Its Utilization in Solar Cells. *ACS Energy Letters* **2019**, *4*, 2137-2143.

- 14. Fu, L.; He, Y.; Zheng, J.; Hu, Y.; Xue, J.; Li, S.; Ge, C.; Yang, X.; Peng, M.; Li, K., et al. TeSe1–Photodiode Shortwave Infrared Detection and Imaging. *Advanced Materials* **2023**, *35*, 2211522.
- 15. Zhou, J.; Zhang, G.; Wang, W.; Chen, Q.; Zhao, W.; Liu, H.; Zhao, B.; Ni, Z.; Lu, J. Phase-engineered synthesis of atomically thin te single crystals with high on-state currents. *Nature Communications* **2024**, *15*, 1435.
- 16. Yang, F.; Li, K.; Fan, M.; Yao, W.; Fu, L.; Xiong, C.; Jiang, S.; Li, D.; Xu, M.; Chen, C., et al. Strongly Anisotropic Quasi-1D BaTiS3 Chalcogenide Perovskite for Near-Infrared Polarized Photodetection. *Advanced Optical Materials* **2023**, *11*, 2201859.
- 17. Zhao, C.; Batiz, H.; Yasar, B.; Kim, H.; Ji, W.; Scott, M. C.; Chrzan, D. C.; Javey, A. Tellurium Single-Crystal Arrays by Low-Temperature Evaporation and Crystallization. *Advanced Materials* **2021**, *33*, 2100860.
- 18. Zhao, C.; Batiz, H.; Yasar, B.; Ji, W.; Scott, M. C.; Chrzan, D. C.; Javey, A. Orientated Growth of Ultrathin Tellurium by van der Waals Epitaxy. *Advanced Materials Interfaces* **2022**, *9*, 2101540.
- 19. Ghosh, G.; Sharma, R. C.; Li, D. T.; Chang, Y. A. The Se-Te (Selenium-Tellurium) system. *Journal of Phase Equilibria* **1994**, *15*, 213-224.
- 20. Wang, Q.; Safdar, M.; Xu, K.; Mirza, M.; Wang, Z.; He, J. Van der Waals Epitaxy and Photoresponse of Hexagonal Tellurium Nanoplates on Flexible Mica Sheets. *ACS Nano* **2014**, *8*, 7497-7505.
- 21. Peng, M.; Yu, Y.; Wang, Z.; Fu, X.; Gu, Y.; Wang, Y.; Zhang, K.; Zhang, Z.; Huang, M.; Cui, Z., et al. Room-Temperature Blackbody-Sensitive and Fast Infrared Photodetectors Based on 2D Tellurium/Graphene Van der Waals Heterojunction. *ACS Photonics* **2022**, *9*, 1775-1782.
- 22. Frolov, T.; Mishin, Y. Thermodynamics of coherent interfaces under mechanical stresses. I. Theory. *Physical Review B* **2012**, *85*, 224106.
- 23. Gabrys, P. A.; Seo, S. E.; Wang, M. X.; Oh, E.; Macfarlane, R. J.; Mirkin, C. A. Lattice Mismatch in Crystalline Nanoparticle Thin Films. *Nano Letters* **2018**, *18*, 579-585.
- 24. Gibbons, T. G. Calculation of the Thermal Expansion for a Quasiharmonic Model of Tellurium. *Physical Review B* **1973**, *7*, 1410-1419.
- 25. Zhao, Y. H.; Lu, K. Grain-size dependence of thermal properties of nanocrystalline elemental selenium studied by x-ray diffraction. *Physical Review B* **1997**, *56*, 14330-14337.
- 26. Masuki, R.; Nomoto, T.; Arita, R.; Tadano, T. Full optimization of quasiharmonic free energy with an anharmonic lattice model: Application to thermal expansion and pyroelectricity of wurtzite GaN and ZnO. *Physical Review B* **2023**, *107*, 134119.
- 27. Chen, C. Q.; Shi, Y.; Zhang, Y. S.; Zhu, J.; Yan, Y. J. Size Dependence of Young's Modulus in ZnO Nanowires. *Physical Review Letters* **2006**, *96*, 075505.
- 28. Lanyon, H. P. D. Optical and Electrical Properties of Selenium Tellurium Alloys. *Journal of Applied Physics* **1964,** *35*, 1516-1523.
- 29. McGuigan, B. C.; Pochet, P.; Johnson, H. T. Critical thickness for interface misfit dislocation formation in two-dimensional materials. *Physical Review B* **2016**, *93*, 214103.
- 30. Beznasyuk, D. V.; Stepanov, P.; Rouvière, J. L.; Glas, F.; Verheijen, M.; Claudon, J.; Hocevar, M. Full characterization and modeling of graded interfaces in a high lattice-mismatch axial nanowire heterostructure. *Physical Review Materials* **2020**, *4*, 074607.
- 31. Seki, T.; Sánchez-Santolino, G.; Ishikawa, R.; Findlay, S. D.; Ikuhara, Y.; Shibata, N. Quantitative electric field mapping in thin specimens using a segmented detector: Revisiting the transfer function for differential phase contrast. *Ultramicroscopy* **2017**, *182*, 258-263.
- 32. Brown, H. G.; Shibata, N.; Sasaki, H.; Petersen, T. C.; Paganin, D. M.; Morgan, M. J.; Findlay, S. D.

Measuring nanometre-scale electric fields in scanning transmission electron microscopy using segmented detectors. *Ultramicroscopy* **2017**, *182*, 169-178.

33. Close, R.; Chen, Z.; Shibata, N.; Findlay, S. D. Towards quantitative, atomic-resolution reconstruction of the electrostatic potential via differential phase contrast using electrons. *Ultramicroscopy* **2015**, *159*, 124-137.



Electronic Supplementary Material

Heterojunction interfacial metallization effects on carrier dynamics in Te-Se based infrared photodiodes: An atomic-resolution structure—property study

Zunyu Liu^{1,§}, Meng Peng^{1,2,6,§}, Ziyang Huang⁵, Yuxuan Hu^{1,3}, Huaiyuan Wang⁵, Maohua Chen¹, Shuwen Yan^{1,2}, Mingyang Liu¹, Ning Ma¹, Jingshu Zhang^{1,2}, Chao Chen^{1,2,3,4,*}, Yihua Gao¹, Shuangfeng Jia⁵, Jianbo Wang⁵, Luying Li^{1,*}, and Jiang Tang^{1,2,3,4}

¹Wuhan National Laboratory for Optoelectronics, Huazhong University of Science and Technology, Wuhan 430074, China

²School of Optical and Electronic Information, Huazhong University of Science and Technology, Wuhan 430074, China

³China-EU Institute for Clean and Renewable Energy, Huazhong University of Science and Technology, Wuhan 430074, China

⁴Optics Valley Laboratory, Wuhan 430074, China

⁵Center for Electron Microscopy, MOE Key Laboratory of Artificial Micro- and

Nano-Structures and the Institute for Advanced Studies, School of Physics and Technology,

Wuhan University, Wuhan 430072, China

⁶School of Microelectronics, Wuhan Textile University, Wuhan 430200, China

*Address correspondence to Chao Chen, cchen@mail.hust.edu.cn; Luying Li, luying.li@hust.edu.cn

Supporting information to https://doi.org/10.26599/NR.2025.94908026

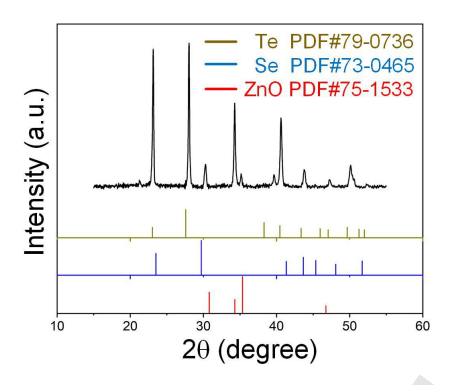


Figure S1 XRD spectra of TeSe alloy/ZnO heterojunctions, the standard PDF spectra for Te, Se, and ZnO are listed below for reference.

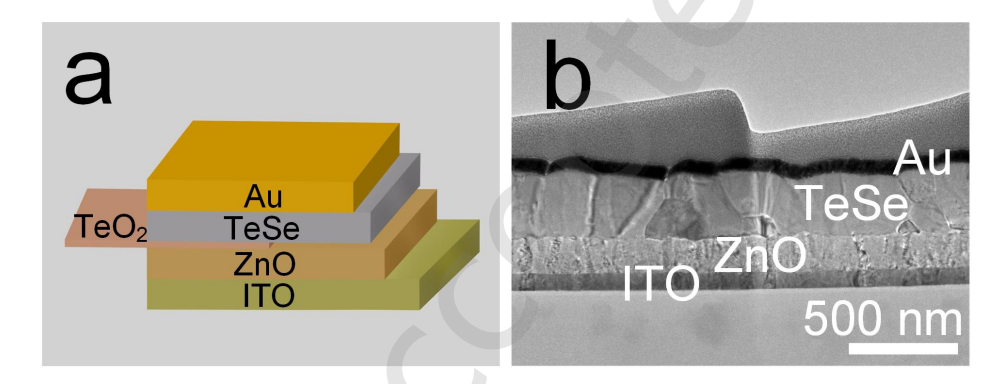


Figure S2 The fundamental characterization of the device. **a** The schematic representation of each functional material layer in a TeSe alloy-based infrared photodiode. **b** TEM image depicting the cross-sectional view of the device.

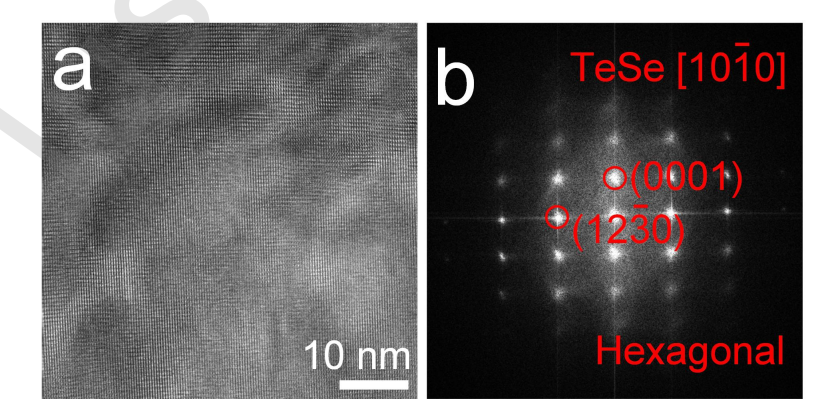


Figure S3 HRTEM image and corresponding FFT of the TeSe alloy projected along $[10\overline{1}0]$ axis.

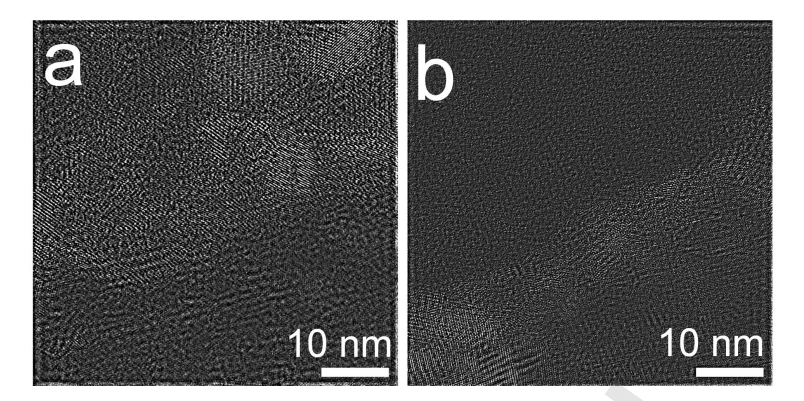


Figure S4 After removing the principal diffraction spots relating to TeSe alloy and ZnO from Fig. 2b and Fig. 2e, the residual lattice information is generated via inverse Fourier transform, with (a) corresponding to the original Fig. 2b and (b) to the original Fig. 2e, respectively.

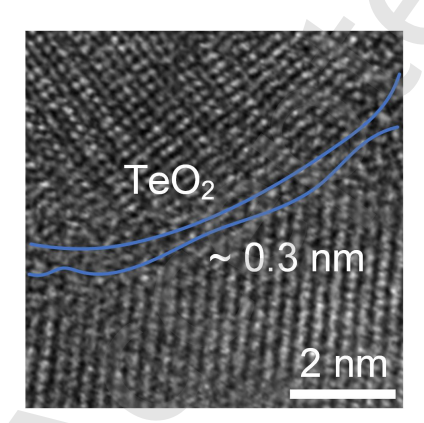


Figure S5 High-resolution HAADF confirmation of TeO2 interfacial layer.

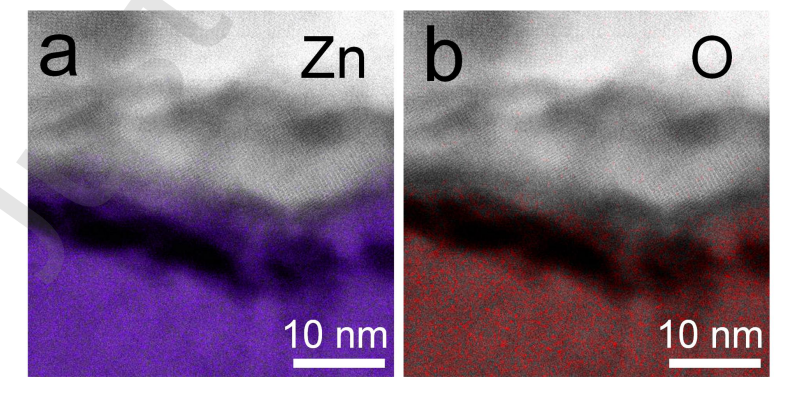


Figure S6 EDS Elemental map of Zn and O at the TeSe/ZnO interface.

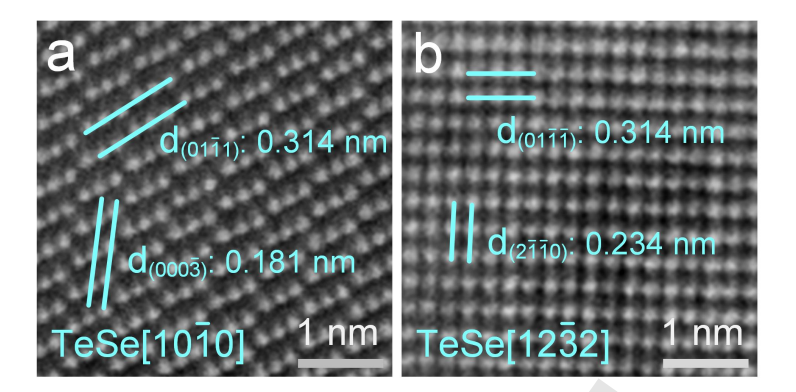


Figure S7 Detailed d-spacing analysis for diffraction spot indexing in Figure 3. (a, b) Enlarged views of the blue dashed box regions from Figure 3(a) and (d), respectively.

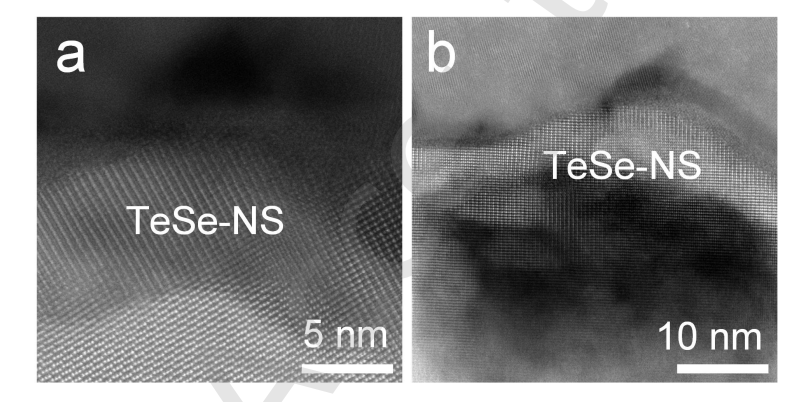


Figure S8 Repeatability verification of the formation of new TeSe structural phases.

Note S1:

The formula for calculating thermal stress is:

$$\sigma = E \cdot \alpha \cdot \Delta T \tag{Equation S1}$$

In this context, σ represents the thermal stress, E denotes the elastic modulus of the material, α is the thermal expansion coefficient, and ΔT is the temperature difference. During the annealing process, ZnO and Te_{0.6}Se_{0.4} crystallize simultaneously at an annealing temperature of 260 °C. The room temperature is 20 °C, resulting in a temperature difference of 240 °C. Based on the differences in thermal expansion coefficients and elastic moduli, the thermal stress in Te_{0.6}Se_{0.4} alloy is calculated to be 81.6 MPa, while that in ZnO polycrystalline is 249.6 MPa. Although the thermal expansion coefficients of Te_{0.6}Se_{0.4} and ZnO are relatively close (with the thermal expansion coefficient of Te_{0.6}Se_{0.4} alloy being approximately 10×10^{-6} K⁻¹ and that of ZnO being 5.2×10^{-6} K⁻¹), the thermal stress in ZnO is substantially higher due to its significantly greater elastic modulus (around 200 GPa, compared to 34 GPa for Te_{0.6}Se_{0.4} alloy).

Note S2:

The stress arising from lattice mismatch is examined next. The structural parameters of each material were determined using X-ray diffraction (XRD), as presented in Fig. S1. The Te structure belongs to hexagonal crystal system with the space group $P3_121$ (152), and the lattice constants are a = b = 0.4456 nm and c = 0.5921 nm. Se also crystallizes with hexagonal structure, with a = b = 0.4367 nm and c = 0.4954 nm, and shares the same space group, $P3_121$ (152). The ZnO structure belongs to hexagonal system with the space group $P6_3$ mc (186), having lattice constants a = b = 0.3351 nm and c = 0.5226 nm. The $Te_{0.6}Se_{0.4}$ alloy, which also adopts hexagonal crystal structure, belongs to the space group $P3_121$ (152), with assumed lattice constants a = b = 0.4420 nm and c = 0.5534 nm. The lattice mismatch is then calculated using the appropriate formula:

$$f = \frac{a_{film} - a_{substrate}}{a_{substrate}}$$
 (Equation S2)

ZnO is used as the substrate in this work, and the TeSe alloy film is deposited on ZnO via thermal? evaporation. For ZnO and $Te_{0.6}Se_{0.4}$, the lattice parameters a and c were calculated. The least lattice mismatch is 5.89 %, while the largest can reach 31.9 %. The Stoyn formula can be used to estimate the stress at the heterojunction.

$$\sigma = \frac{E_{film}}{1 - \nu_{film}} \cdot f$$
 (Equation S3)

 E_{film} and v_{film} stand for the film's Young's modulus and Poisson's ratio, respectively. According to verification studies, Te has a matching Poisson's ratio of $v_{Te} \approx 0.22$. The Poisson's ratio for Se is $v_{Se} \approx 0.2$. Based on the composition of the alloy, the estimated Young's modulus for the Te_{0.6}Se_{0.4} alloy is $E_{Te0.6Se0.4} = 34$ GPa and the Poisson's ratio is $v_{Te0.6Se0.4} \approx 0.21$. Rough estimates place the interface stress in the range of 2.53-13.73 GPa.